


Influence of the droplet trajectory on the resulting droplet deformation and droplet size distribution in high-pressure homogenizer orifices

Felix Johannes Preiss¹  | Eva Rütten¹ | Alexander Tröster¹ | Volker Gräf² | Heike Petra Karbstein¹

¹Institute of Process Engineering in Life Sciences, Food Process Engineering, Karlsruhe Institute of Technology (KIT), Karlsruhe, Germany

²Department of Food Technology and Bioprocess Engineering, Max Rubner-Institut (MRI), Federal Research Institute of Nutrition and Food, Karlsruhe, Germany

Correspondence

Felix Johannes Preiss, Institute of Process Engineering in Life Sciences, Food Process Engineering, Karlsruhe Institute of Technology (KIT), Karlsruhe, Germany.
Email: felix.preiss@kit.edu

Heike Petra Karbstein, Institute of Process Engineering in Life Sciences, Food Process Engineering, Karlsruhe Institute of Technology (KIT), Karlsruhe, Germany.
Email: heike.karbstein@kit.edu

Funding information

Deutsche Forschungsgemeinschaft, Grant/Award Numbers: 265685259, 425332181

Abstract

High-pressure homogenization is a commonly used process to produce emulsions with a droplet size of less than 1 μm . During the process, a pre-emulsion is pumped with a pressure of several mega Pascal through a disruption unit, where the droplets are deformed and subsequently broken up in the turbulent area of the disruption unit. The scope of this investigation is to determine the influence of the droplet trajectory on the droplet size distribution of emulsions of different viscosity ratios or interfacial tension. Measurements of the droplet deformation prior to the droplet breakup using image-processing tools complemented the observations. In addition, computational fluid dynamics simulations were performed to determine the stress history on the droplet trajectories. It was found that droplets on a trajectory close to the wall are more deformed when leaving the disruption unit compared to droplets on the centreline. The deformation of droplets at the edge of the jet increases downstream the disruption unit until it is finally disrupted. The simulation results support the experimental data, as it can be shown that shear and strain stresses on the trajectories close to the wall significantly exceed the stresses on the trajectories on the centreline. For an emulsion with a viscosity ratio greater than 3, droplets on a trajectory close to the wall resulted in smaller droplets and narrower droplet size distribution, while no significant influence was found for smaller viscosity ratios. Lowering the interfacial tension results in a stronger deformation, which was more pronounced for lower viscosity ratios ($\lambda \approx 3$).

KEYWORDS

computational fluid dynamics, droplet deformation, droplet trajectory, high-pressure homogenization, stress history

This is an open access article under the terms of the Creative Commons Attribution License, which permits use, distribution and reproduction in any medium, provided the original work is properly cited.

© 2022 The Authors. The *Canadian Journal of Chemical Engineering* published by Wiley Periodicals LLC on behalf of Canadian Society for Chemical Engineering.

1 | INTRODUCTION

Emulsions can be found in food, cosmetic, and pharmaceutical products. Emulsions with droplet sizes smaller than 1 μm and a low to medium viscosity of less than 200 $\text{mPa} \cdot \text{s}$ are most commonly produced using a high-pressure homogenization process.^[1] During the process, a pre-emulsion with large droplets is pumped through a disruption unit where the flow is accelerated by the reduced cross-section. A flat valve most frequently realizes the reduction of the cross-section in production scale high-pressure homogenizers. In this investigation, an orifice is used as a model disruption unit geometry due to its better optical accessibility. The droplets in the pre-emulsion are exposed to shear stresses and elongational strain when passing the disruption unit due to the accelerating flow. These stresses result in droplet deformation and finally, when the deformed droplets enter the turbulent shear layer of the emerging jet, in their breakup into many small droplets due to viscous and/or inertia stresses.^[2] The flow in the orifice can be characterized using the Reynolds number:

$$Re_{\text{orifice}} = \overline{u_{\text{orifice}}} \cdot D \cdot \rho / \eta_c \quad (1)$$

where $\overline{u_{\text{orifice}}}$ is the average velocity in the orifice, D is the orifice diameter, ρ is the density of the continuous phase, and η_c is the dynamic viscosity of the continuous phase.

First investigations on the droplet deformation in laminar shear or extensional flow were conducted by Taylor,^[3,4] who found that the deformation depends on the capillary number Ca and viscosity ratio λ . These two dimensionless numbers are defined as follows:

$$\lambda = \eta_d / \eta_c \quad (2)$$

$$Ca = \tau \cdot d / (4 \cdot \gamma) \quad (3)$$

$$\tau = \eta_c \cdot (|\dot{\epsilon}| + |\dot{\gamma}|) \quad (4)$$

where η_d is the dynamic viscosity of the dispersed phase, η_c is the dynamic viscosity of the continuous phase, τ is the stress acting on the droplet, d is the droplet diameter, γ is the interfacial tension, $\dot{\epsilon}$ is the elongation rate, and $\dot{\gamma}$ is the shear rate. Taylor showed that the droplet deformation increases proportionally when Ca is increased, while the slope of the increase depends on the viscosity ratio. When a critical capillary number Ca_{crit} is exceeded, the droplet does not reach a stationary shape anymore and is continuously deformed until it breaks up, wherein the critical capillary number depends on the viscosity ratio and the flow type.^[5] Furthermore, it was found that in the case of high interfacial tensions and low viscosity

ratios in pure shear flow and low stresses ($Ca < 0.5$), the deformation depends on the capillary number only. In the case of high viscosity ratios and low interfacial tensions, the deformation depends on λ^{-1} . Cox^[6] and Elmendorf^[7] extended this correlation to laminar extensional flow and higher deformations ($b_0 \geq 2$) where the deformation ratio b_0 is defined as follows:

$$b_0 = d_1 / d_0 \quad (5)$$

where d_1 is the length of the major axis of the emerging ellipsoid and d_0 is the diameter of the undeformed droplet.

Brösel and Schubert^[8] used emulsification experiments to determine the influence of an emulsifier on the droplet deformation process. They assumed, based on their findings, that hardly any emulsifier was adsorbed during the droplet-breakup process. They found that the droplet sizes do not decrease proportionally when the interfacial tension is decreased. Furthermore, Brösel and Schubert^[8] used a scaled, optically accessible disruption unit to visualize the droplet breakup process. It was found that an emulsifier did not alter the droplet deformation qualitatively.

Droplet deformation in an optically accessible step-type orifice was evaluated by Kelemen et al.^[9] They found that the droplets are supercritically ($Ca > Ca_{\text{crit}}$) deformed in the inlet and only break up downstream of the orifice exit. Walzel^[10] simulated the droplet deformation inside a passage through an orifice on the centreline using an approach stated by Cox^[6] and Kalb et al.^[11] These findings were later validated using experimental data from a scaled orifice setup whereby a good agreement was found between the simulation and the experiment at limited settings.^[12]

Among others, Feigl et al.^[13] and Hövekamp^[14] used computational fluid dynamics (CFD) simulations to determine the stress history on the droplet streamline with changing stress loads and constant interfacial tension, which was subsequently correlated with the droplet deformation from simulations and experimental data. In all investigated setups, droplets that travel on a trajectory close to the wall are exposed to higher stresses and are thus more deformed.

Mutsch et al.^[15] conducted a first investigation on the influence of droplet deformation on the resulting droplet size distribution using a scaled high-pressure homogenization setup. The analysis showed that droplets on a trajectory close to the wall resulted in slightly smaller droplets after passing through the disruption unit.

The target of this contribution is to identify the influence of droplet trajectory and emulsion material parameters (viscosity ratio and interfacial tension) on the droplet size distribution of homogenized emulsions. Differences will subsequently be correlated with changes in the droplet deformation b prior to droplet breakup and its stress

history. The stress history is determined using CFD tools according to Håkansson et al.^[16] Simulation of stress history and optical results on droplet deformation was used to improve the understanding of droplet deformation and breakup under fast-changing stresses, as found in typical high-pressure homogenizer disruption units.

2 | MATERIALS AND METHODS

2.1 | Materials

For droplet visualization, a transparent mixture of demineralized water and glycerol (purity 99.5%, SuboLab GmbH, Pfinztal-Söllingen, Germany) in a mass ratio of 41:59 was used as a continuous phase. In addition, 0.5 wt.% polysorbate 20 (Tween 20[®], Carl Roth, Karlsruhe, Germany) is added when the droplet deformation with reduced interfacial tension is investigated. Furthermore, 0.2 wt.% potassium sorbate (VWR International GmbH, Darmstadt, Germany) and 0.1 wt.% citric acid (Carl Roth GmbH + Co. KG, Karlsruhe, Germany) were always added for preservation, as the fluid is used multiple times. This mixture has a density of 1150.4 kg · m⁻³ and a viscosity of 9.42 ± 0.01 mPa · s with Newtonian flow behaviour.

For measurements of the resulting droplet size distribution, a demineralized water-maltodextrin solution with

0.5 wt.% polysorbate 20 (Tween 20[®], Carl Roth, Karlsruhe, Germany) is used as a continuous phase. The water-glycerol system could not be used for measurements of the droplet size distribution as it induced self-emulsification effects as described by Shah et al.^[17] that disturbed optical analysis. The weight fractions of all used components for the continuous phases are presented in Table 1. This resulted in a mixture with a density of 1103.6 kg · m⁻³, a viscosity of 8.808 ± 0.032 mPa · s with Newtonian flow behaviour, and a refractive index of 1.373 whereby all parameters were measured at a temperature of 20°C.

The disperse phase consists of a mixture of a middle-chain-triglyceride oil and 120 ppm (w) Nile red dye (9-(diethyl-amino)benzo[a]phenoxazin-5(5H)-one, Sigma-Aldrich Chemie GmbH, Taufkirchen, Germany) where the oil was either Miglyol 840[®] (IOI Oleo GmbH, Witten, Germany) with a viscosity of 10.1 ± 0.03 mPa · s and a refractive index of 1.442, or Miglyol 812[®] (IOI Oleo GmbH, Witten, Germany) with a viscosity of 29.1 ± 0.06 mPa · s and a refractive index of 1.449, or Miglyol 829[®] (IOI Oleo GmbH, Witten, Germany) with a viscosity of 235.1 ± 3.34 mPa · s and a refractive index of 1.456. For all static light scattering measurements, 0.001 was used as an imaginary part of the refractive index for all oils/emulsions, following the guidelines of Malvern Panalytical Ltd.^[18] An overview of all material properties is presented in Table 2.

TABLE 1 Composition of all used continuous phases

	Weight fraction (-)					
	Glycerol	Demineralized water	Maltodextrin	Polysorbate 20	Potassium sorbate	Citric acid
Droplet size distribution measurement	0	74.1	25.4	0.5	0	0
Droplet visualization	58.53	40.67	0	0.5	0.2	0.1
	58.82	40.88	0	0	0.2	0.1

TABLE 2 Resulting viscosity ratios and interfacial tensions for droplet size distribution measurements and droplet visualization analysis

	Emulsifier fraction (wt.%)	Viscosity ratio λ (-)	Density continuous phase (kg m ⁻³)	Density disperse phase (kg m ⁻³) ^a	Interfacial tension γ (mN m ⁻¹) ^b		
Droplet size distribution measurement	0.5	1.15	1103.59 ± 0.18	918	1.94 ± 0.02		
		3.30			2.36 ± 0.04		
		26.7			1.70 ± 0.11		
Droplet visualization	0.5	3.09	1150.61 ± 0.49	943	3.20 ± 0.04		
		0			15.52 ± 0.20		
	0	0.5			25	1008	2.77 ± 0.15
		0					13.80 ± 0.22

^aAccording to supplier's information.

^bEquilibrium value.

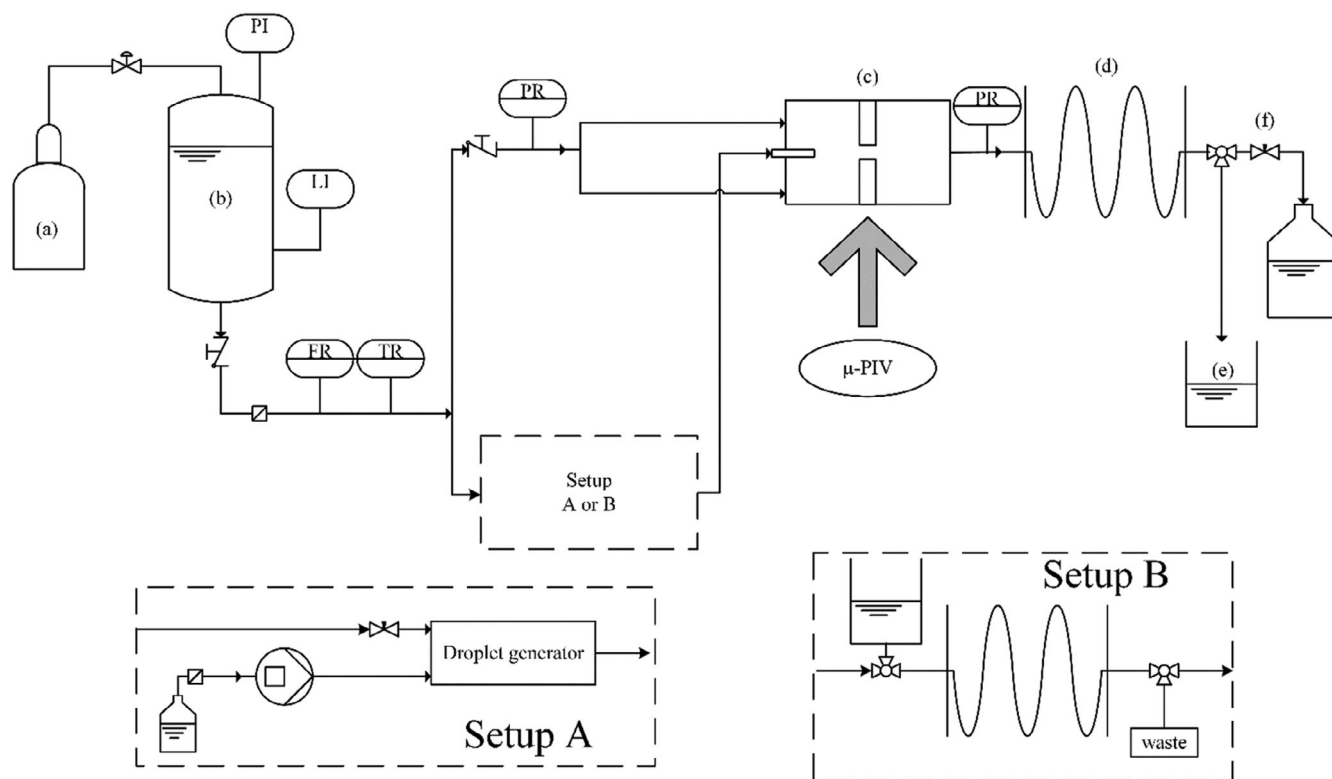


FIGURE 1 Experimental setup with setup A for droplet deformation visualization and setup B for droplet size distribution measurements

Measurements of the rheological properties were performed with a rotational rheometer (Anton Paar, Physica MCR 101, Graz, Austria) at a temperature of 20°C. The density was determined using a density determination set DIS 11 (DCAT11, DataPhysics, Filderstadt, Germany) at a temperature of 20°C. Interfacial tension measurements are conducted with a Wilhelmy plate (DCAT11, DataPhysics) and an OCA 15 LJ (DataPhysics Instruments GmbH, Filderstadt, Germany) at a temperature of 20°C.

2.2 | Experimental setup

Depicted in Figure 1 is the experimental setup of a high-pressure homogenization process with an optically accessible orifice, which is used to determine the droplet deformation and the resulting droplet size distribution. The scaling approach for the experimental setup is presented by Preiss et al.^[19] The continuous phase is stored in a pressure vessel (b) which is pressurized with a nitrogen gas cylinder (a) to ensure a pulsation-free flow. During an experiment, the volume flow, the temperature, as well as the inlet and the outlet pressure of the orifice are recorded continuously. The stream of the continuous phase is separated in the main stream, which goes directly to the optically accessible orifice (c), and a side stream. In the side

stream, either a monodisperse pre-emulsion with a low disperse phase fraction is produced using a droplet generator (setup A) or a pre-emulsion with a high disperse phase fraction, which was produced with a rotor-stator-machine (propeller stirrer or disperser T25 Ultra-Turrax® IKA®-Werke GmbH & Co. KG, Staufen, Germany), is filled in a pipe coil (setup B). Two different setups were necessary as, on the one hand, the low dispersed phase fraction of droplet generator (setup A) does not allow droplet size measurements using the static light scattering method, and on the other hand, the setup B has a wide droplet trajectory range and the initial droplet size of the deformed droplet downstream the orifice is unknown, which impedes the correlation of the droplet deformation with the stress history on the trajectory. Besides, the droplets entered the flow in the inlet channel across the whole cross-section of the positioning capillary when a pre-emulsion in setup B was used. When the droplet generator was used in setup A, however, the droplets enter the inlet channel on one specific trajectory with minimal variance, as presented by Preiss et al.^[20] The pre-emulsion was conducted with the rotor-stator-machine with a viscosity ratio of $\lambda = 1.16$ having a Sauter mean diameter of $d_{3,2} = 10.96 \pm 1.23 \mu\text{m}$, the pre-emulsion with a viscosity ratio of $\lambda = 3.30$ having a Sauter mean diameter of $d_{3,2} = 15.19 \pm 2.46 \mu\text{m}$, and the pre-emulsion with a viscosity ratio of $\lambda = 33.0$ having a

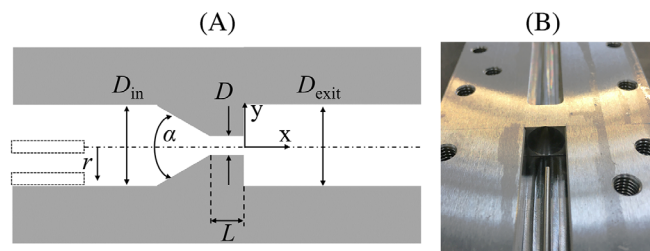


FIGURE 2 (A) Sketch of the top view of the orifice with inserted capillary with all relevant dimensions and (B) image of the optically accessible orifice with capillary on the centreline

Sauter mean diameter of $d_{3,2} = 12.74 \pm 0.65 \mu\text{m}$. The droplet generator is described in detail by Preiss et al.^[20] The side stream with the pre-emulsion is reinjected in front of the optically accessible orifice using a 1/16" stainless steel capillary with an inner diameter of 1 mm (Chromatographie Handel Müller GmbH, Fridolfing, Germany). The capillary was either placed on the centreline of the inlet channel or close to the wall. When measuring the resulting droplet size distribution, the sample-collecting hose (d) can be drained into the sample collecting beaker (e). During all experiments, a Thoma number of 0.3 is set using a needle valve (f) to completely suppress cavitation.^[21]

$$Th = p_{bp}/p_{in} \quad (6)$$

where p_{in} is the pressure in the inlet channel and p_{bp} is the backpressure in the outlet channel.

The flow channel of the optically accessible orifice was milled into two stainless steel blocks, which were subsequently glued together as depicted in Figure 2B. An acrylic glass plate was pressed on the flow channel using a steel frame to seal the channel. The inlet and outlet channels had a dimension of $10 \text{ mm} \times 10 \text{ mm}$, where the edge length was defined as the parameters D_{in} and D_{exit} , respectively. The drilling hole of the orifice had a diameter D of 1 mm and a length L of 2 mm. The inlet channel and the drilling hole were connected by a conical inlet with an angle α of 60° . The capillary was placed either on the centreline or close to the wall. The position of the capillary and thus the trajectory of the droplets are defined with the parameter r^* as follows:

$$r^* = r/(D_{in}/2) \quad (7)$$

where r is the distance from the trajectory to the centreline. A sketch of the orifice with previously mentioned parameters is depicted in Figure 2A.

2.3 | Determination of the resulting droplet size distribution

To determine the resulting droplet size distribution, the experimental setup was initially operated only with the continuous phase until the steady state with the desired flow conditions was reached. Afterwards, the flow was stopped, and the pre-emulsion was filled from the beaker into the pipe coil in the side stream. Subsequently, the flow was restarted, and a sample was collected from the hose (d) when the pre-emulsion passed through the orifice. The droplet size distributions are determined afterwards by static light scattering using a Malvern Mastersizer 2000 with a helium-neon laser (633 nm) in combination with a blue light diode (466 nm) as light sources and a Hydro 2000 μP sample dispersion unit (Malvern Panalytical Ltd., Malvern, the United Kingdom). The stirrer was switched off when the sensitive pre-emulsion was measured, and the stirrer was set to 1500 min^{-1} when the process samples were measured. Every parameter combination was addressed three times, and the droplet size distribution of every sample was measured 3×3 times. The software OriginPro 2019 (OriginLab Corp., Northampton, MA, USA) was used to calculate the average droplet size distribution of every parameter combination, including standard deviations.

2.4 | Droplet visualization

When investigating the droplet deformation after leaving the orifice, a mono-disperse pre-emulsion with a droplet diameter d_0 of about $200 \mu\text{m}$ was produced in the side stream using the droplet generator. The fluorescence-labelled droplets were visualized using the high-speed camera and the laser of a micro-particle image velocimetry measurement ($\mu\text{-PIV}$) setup, which consisted of a high-speed double frame camera (FlowSense 4M Camera Kit, Dantec Dynamics, Skovlunde, Denmark) with a 12-bit resolution, 2048×2048 pixels, and a double-pulsed neodymium-doped yttrium aluminum garnet (ND:YAG) laser (Dual-Power 30–15 of Dantec Dynamics, Skovlunde, Denmark). Double frame images were taken at a frequency of 7.4 s^{-1} , and the time between the two frames was set to $100 \mu\text{s}$. The laser and camera were attached to a microscope (Dantec HiPerformance Microscope, Skovlunde, Denmark), which had a resulting magnification of $1.75\times$ using an objective lens (HC Plan Fluotar 2.5 \times /0.07, Leica Microsystems Wetzlar GmbH, Wetzlar, Germany) and a $0.5\times$ camera adapter. This resulted in a field of view of about $12 \text{ mm} \times 12 \text{ mm}$ with a spatial resolution of $6 \mu\text{m}/\text{px}$.

A first image-processing step was done with the commercial software Dynamic Studio 6.10 (Dantec Dynamics,

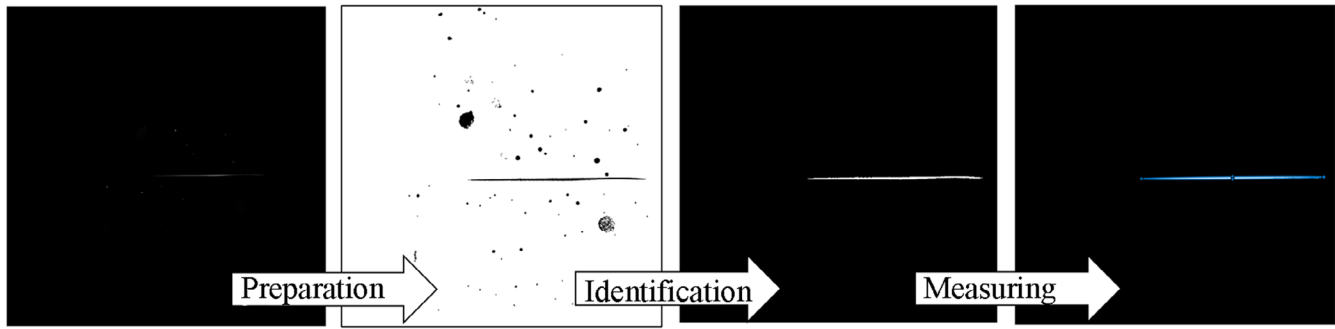


FIGURE 3 Visualization of the major image analyzing steps to identify a deformed droplet, which is depicted as a horizontal thin thread in the middle of each image

Skovlunde, Denmark), where an average image is calculated from all images of one experimental run that was subsequently subtracted from the images to remove the background. All the following image-processing steps were performed with MATLAB 2019b (MathWorks, Nantucket, MA, USA).

The image processing in MATLAB was executed in three major steps: preparation, identification, and measuring as pictured in Figure 3. At first, the brightness was adjusted to improve droplet visibility. After that, to reduce background noise, every object with an area of less than 200 pixels was removed from the image. In the following subordinate step, the image was binarized to obtain a defined border between droplet and background. In order to be able to work with MATLAB's image-processing tools in subsequent stages, the image had to be inverted.

Two methods were used to distinguish between droplets and objects from the backflow area surrounding the jet, due to the fact that less deformed droplets were harder to identify. Under operation conditions, for example, small Reynolds numbers and high viscosity ratios, where the deformation ratio b is smaller than 10, droplets are recognized by their circularity and location. The deformation b is defined as

$$b = d_1/d_2 \quad (8)$$

where d_2 is the length of the minor axis of the emerging ellipsoid.

The cutoff for circularity had to be manually altered for every setting between 0.75–0.35 (0 = perfect circle) based on the smallest circularity out of 10 analyzed droplets. Still misleadingly identifying too many objects as droplets, another filter was added, which removed elements that left the centre plain in relation to the orifice by more than 1000 μm in both negative and positive y direction. Additionally, the filter for removing objects with an area of less than 200 pixels was increased to

500 pixels as well. Under operation conditions where elongation ratios are greater than 10, droplets are spotted by criteria like porosity and circularity, as described in detail by Preiss et al.^[22] Droplets in the backflow area around the jet often appeared noisy, therefore objects with a porosity greater than 0.1 (0 = not porous) were eliminated. Droplets with higher elongation ratios were heavily lengthened, hence setting the cutoff for circularity to 0.7 was sufficient. For both high and low elongation ratios, the edges of remaining objects are smoothed in the last intermediate step to improve measuring accuracy.

To determine droplet size and position, ellipses were adapted to droplets where the long axis was registered as droplet length and the short axis as width. The centre of mass was taken to determine droplet position relative to the orifice. To further eliminate droplets that were not depicted correctly, either because they leave the image or because they were partially concealed by the orifice, a filter was added, which removes droplets that were less than 100 μm away from the right image border or closer than 350 μm to the orifice. The latter distance was determined to be larger due to a reflection caused by the metallic channel that "splits" the droplets, therefore inducing sorting problems. Droplets that were deformed perpendicular to the flow direction were removed as well, since they could have left the image plain, resulting in an incorrect droplet length if measured by the mentioned method. For this purpose, all pixels in the ellipse were counted and divided by the number of pixels of the smallest possible surrounding box. For this ratio, a cutoff of 0.8 was chosen after analyzing 300 distorted and undistorted droplets.

2.5 | CFD simulations of stress history on selected trajectories

To determine the stress history of the droplets along different streamlines distributed on the cross-section of the

TABLE 3 Boundary conditions for a Reynolds number $Re_{\text{orifice}} = 1000$

Re_{orifice} (-)	Initial relative pressure p_{in} (Pa)	Mass flow rate \dot{m}_{in} (kg s ⁻¹)	Relative outlet pressure p_{bp} (Pa)
1000	131 400	0.007 69	67 600

geometry, CFD simulations were used. The flow is simplified and assumed to be single-phase, so that only the continuous phase is simulated. The stress history is recorded by particle tracking of massless particles along the flow. Simulations were carried out using ANSYS fluent version 2020R2. The single-phase, incompressible, isothermal, Newtonian, and continuous flow assumptions were used for the simulation. The modelling of the turbulence is carried out according to the Reynolds Averaged Navier Stokes (RANS) approach. The realizable k-epsilon model was used based on the investigations conducted by Håkansson et al.^[16]

2.5.1 | Geometry and mesh

The geometry of the disruption unit is derived from the experimental setup of the optically accessible orifice. Since the simulation only considers the stresses in the inlet part of the geometry at the point between leaving the capillary and the exit of the orifice, the flow was only modelled up to 5 mm after the orifice exit. The computational mesh consists of 31.4 million cells of type poly-hexcore. In the region downstream of the capillary, the conical inlet, and the orifice, the mesh was refined using multiple bodies of influence with a minimum grid length of 0.005 mm. A mesh independence study was performed successfully.

2.5.2 | Materials and boundary conditions

Material values and boundary conditions were determined using experimental data. The density and viscosity were specified for the fluid, taking temperature into account. The inlet was defined as a mass flow inlet. A pressure outlet was specified at the outlet. The used data can be taken from Table 3. A turbulent intensity of 5% and a backflow turbulent viscosity ratio of 10 were assumed at both the inlet and the outlet of the geometry. At all walls, a shear condition of no slip was specified.

2.5.3 | Numerical methods and discretization

A pressure-based solver was chosen to model the continuous phase flow. The simulation was performed in

a steady state. The pressure-velocity coupling was realized using the SIMPLE algorithm. Gradient discretization was performed using the Least Square Cell Based method, and the Second Order scheme was used for pressure discretization. Momentum, turbulent kinetic energy, and turbulent dissipation rate were discretized using the Second Order Upwind scheme.

2.5.4 | Convergence

In addition to the residuals, the area weighted average of the inlet pressure and the area weighted average of the turbulent kinetic energy on different planes perpendicular to the flow direction were considered to evaluate the convergence. The planes are shown in Figure 4. The simulation was assumed convergent once the residuals for convergence, the three velocity components, turbulent kinetic energy, turbulent dissipation, and all other convergence criteria fell below a value of 10^{-4} .

2.5.5 | Postprocessing

Following the flow field calculation, three streamlines were generated. The beginning of the streamlines (blue dots followed by blue thin horizontal lines in Figure 4) corresponds to the exit of the capillary in the experiment. The streamlines are located at the dimensionless distances $r^* = 0, 0.47, \text{ and } 0.94$ to the centreline. The location of the streamlines can be taken from Figure 4. The elongation rate $\dot{\epsilon}$, shear rate $\dot{\gamma}$, and residence time t were calculated along the streamlines. Elongation rate and shear rate are defined as follows:

$$\dot{\epsilon} = \sqrt{\left(\frac{\partial \bar{u}}{\partial x}\right)^2 + \left(\frac{\partial \bar{v}}{\partial y}\right)^2 + \left(\frac{\partial \bar{w}}{\partial z}\right)^2} \quad (9)$$

$$\dot{\gamma} = \sqrt{\left(\frac{\partial \bar{v}}{\partial x} + \frac{\partial \bar{w}}{\partial x}\right)^2 + \left(\frac{\partial \bar{u}}{\partial y} + \frac{\partial \bar{w}}{\partial y}\right)^2 + \left(\frac{\partial \bar{u}}{\partial z} + \frac{\partial \bar{v}}{\partial z}\right)^2} \quad (10)$$

where \bar{u} , \bar{v} , and \bar{w} are the averaged velocity components based on the RANS equations.

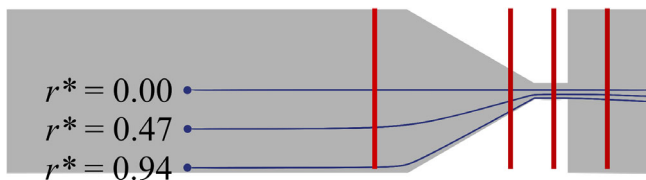


FIGURE 4 Position of the streamlines (blue thin horizontal lines) and the planes (red thick vertical lines) in the geometry to evaluate the convergence

3 | RESULTS

3.1 | Resulting droplet size distribution

During high-pressure homogenization, droplets are deformed by shear stresses and elongational strain in the inlet area of the disruption unit. Subsequently, they are broken by inertia and viscous forces in the turbulent shear layer. Mutsch et al.^[15] have shown in an upscaled model that droplets on a trajectory close to the wall resulted in smaller droplets following the breakup, as the more stretched droplets can probably be broken up more easily. It is hypothesized that smaller droplets emerge from droplets that flow close to the wall compared to droplets flowing on the centreline independent of the viscosity ratio.

Figure 5 compares the resulting droplet sizes of emulsions travelling either on a trajectory close to the wall ($0.75 \leq r^* \leq 1$) or on the centreline ($0 \leq r^* \leq 0.23$) with a viscosity ratio λ of 1.16, 3.30, and 26.7 at $Re_{\text{orifice}} = 4000$. At all process conditions, the minimal droplet diameter was about $0.7 \mu\text{m}$. The emulsion with the highest viscosity ratio of $\lambda = 26.7$ resulted in the widest droplet size distribution. When comparing the droplet size distributions of the two trajectory ranges, significant differences were found only for bigger droplets ($d \geq 7 \dots 10 \mu\text{m}$). In this size range, smaller droplets resulted from the emulsion travelling on the trajectory close to the wall ($0.75 \leq r^* \leq 1$) compared to the emulsion travelling on the centreline ($0 \leq r^* \leq 0.23$). Thus, a narrower droplet size distribution was achieved on the trajectory close to the wall. When turning to the medium viscosity ratio ($\lambda = 3.30$), smaller droplet sizes were produced in comparison to the high viscosity ratio. The emulsion on the trajectory close to the wall again resulted in smaller droplets than those on the centreline. Similar as with the high viscosity ratio, the deviations started at larger droplets ($d \geq 5 \dots 7 \mu\text{m}$), resulting in a narrower droplet size distribution. The emulsion with the lowest viscosity ratio ($\lambda = 1.15$) produced the smallest droplets. However, no significant differences in the droplet size distributions were found for the trajectories close to the wall ($0.75 \leq r^* \leq 1$) and on the centreline ($0 \leq r^* \leq 0.23$).

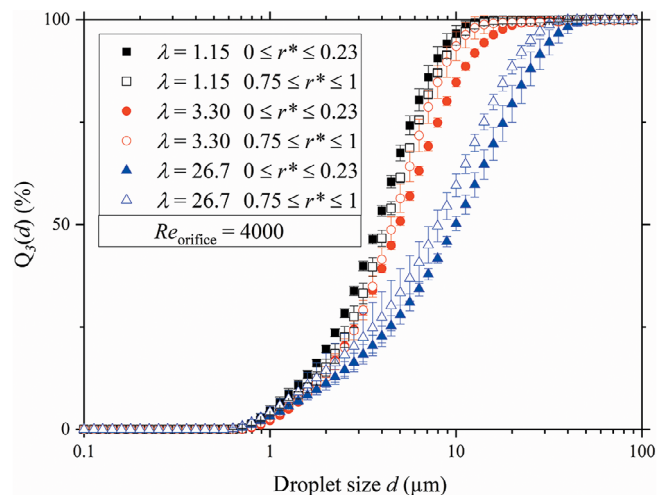


FIGURE 5 Resulting droplet size distribution at a Reynolds number of $Re_{\text{orifice}} = 4000$ of droplets travelling on a trajectory close to the wall (hollow symbols) or on the centre line (solid symbols)

3.2 | Resulting droplet deformation

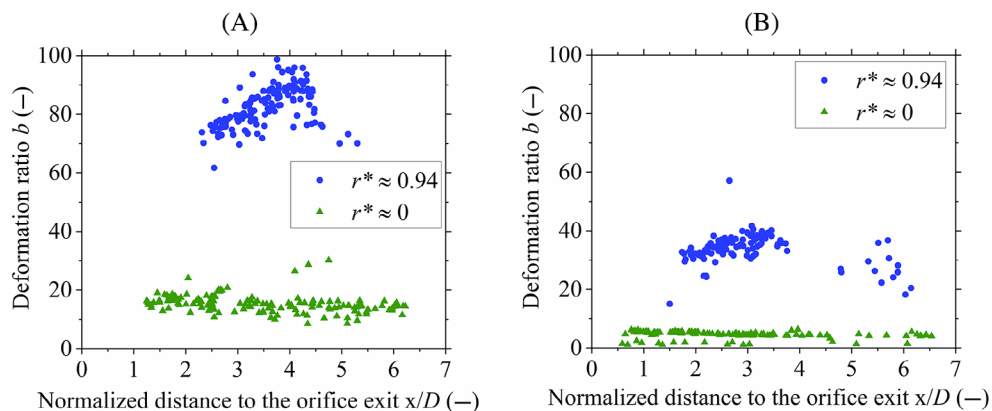
In the following, the findings on the droplet size distribution shall be explained with the droplet deformation prior to breakup. In general, it is expected that smaller droplets are a result of stronger deformed droplets as the droplet thread diameter is closer to the vortex size in the turbulent shear layer of the jet. As a parameter influencing droplet deformation, the interfacial tension is varied in these experiments.

3.2.1 | Influence of trajectory

Droplets are exposed to shear stresses and elongational strain when flowing through the orifice, which results in a deformation. As large areas with high shear and strain rates are located close to the wall, it is hypothesized that droplets that flow on a trajectory close to the wall are more deformed compared to droplets that flow on a centreline trajectory.

Image-processing methods were used to determine the resulting deformation ratio b of the droplets in the outlet channel of the orifice prior to droplet breakup. The resulting deformation ratio b of droplets with a trajectory close to the wall and a centreline trajectory are presented in Figure 6A for an interfacial tension of $\gamma = 3.20 \text{ mN} \cdot \text{m}^{-1}$ (0.5 wt.% emulsifier, see Table 2). The usage of the droplet generator allows the placement of the droplets on a specific trajectory with minimal variance in the location of the trajectory. Every symbol in the cloud represents one correctly depicted droplet. Deformed droplets

FIGURE 6 Resulting droplet deformation ratio at $Re_{\text{orifice}} = 1000$, $\lambda = 3.09$, and $d_0 \approx 200 \mu\text{m}$ with an interfacial tension of (A) $\gamma = 3.20 \pm 0.04 \text{ mN} \cdot \text{m}^{-1}$ or (B) $\gamma = 15.52 \pm 0.20 \text{ mN} \cdot \text{m}^{-1}$



were found in the distance range of $1.2 \leq x/D \leq 6.4$ for droplets travelling on a trajectory on the centre axis ($r^* \approx 0$). Deformed droplets that were closer to the orifice exit or further downstream were not depicted correctly and were therefore excluded from the analysis. These droplets were either partially in the optically inaccessible part of the orifice or already deformed perpendicular to the travelling direction due to interaction with the vortices in the shear layer of the emerging free jet. The resulting deformation ratio b was in the range of $10 < b < 20$. Only isolated droplets had a deformation ratio greater than 25. The deformation did not change with an increasing distance from the orifice exit until breakup was detected. The average deformation ratio of all droplets with a centreline trajectory was 15.3 ± 3.1 .

When turning to the droplets that travelled on a trajectory close to the wall ($r^* = 0.94$), deformed droplets were found in the distance range $2 \leq x/D \leq 5.5$. As droplets on a trajectory close to the wall entered the shear layer of the free jet, where they started to break up earlier compared to droplets on the centreline, only a few droplets were found at a normalized distance greater than 4.5. In general, the deformation ratio of droplets close to the wall was more scattered and significantly increased in comparison to droplets on the centreline. The average deformation ratio for all droplets on a trajectory close to the wall was $b = 82.5 \pm 6.9$ with values between 70–100. In contrast to droplets on the centreline, it was found that the deformation ratio was rising with increasing distance from the orifice exit.

3.2.2 | Influence of interfacial tension

During droplet deformation and breakup, external stresses compete with inner strength forces, which try to maintain the spherical shape. The inner strength forces are mostly dominated by the capillary pressure, which is proportional to the interfacial tension γ . As the

Ca -number is inversely proportional to the interfacial tension (see Equation (3)), droplet deformation ratio b should decrease when increasing the interfacial tension. For this purpose, the droplet deformation was investigated with and without the addition of a fast emulsifier, whereby the emulsifier should adsorb at the interface and result in a lower interfacial tension. However, it has to be taken into account that the emulsifier probably will not adsorb fast enough to reach the equilibrium interfacial tension and furthermore that Gibbs–Marangoni effects may cause interfacial gradients. In the following, the results will be distinguished by the presence or absence of an emulsifier.

The resulting deformation ratio b of droplets in the outlet channel, having travelled either on a trajectory close to the wall or on the centreline with increased interfacial tension ($\gamma = 15.52 \text{ mN} \cdot \text{m}^{-1}/0 \text{ wt.}\%$ emulsifier added), is depicted in Figure 6B. Compared to droplets with an added emulsifier (see Figure 6A), the first deformed droplets could be detected at distances closer to the orifice as they were less deformed (see Figure 6B). On the centreline, deformed droplets were found in the distance range $0.5 \leq x/D \leq 6.5$ with the majority of the droplets showing a deformation ratio of ≈ 4.6 . As for the results with added an emulsifier, the deformation did not change significantly with the normalized distance from the orifice exit, only a tendency to a slight relaxation can be noticed. The deformation ratio of droplets is less scattered compared to droplets when an emulsifier is added, as depicted in Figure 6A. The average deformation ratio was $b = 4.6 \pm 1.3$, see Table 4. When comparing the deformation of droplets with and without added emulsifier (see Figure 6A vs. 6B), it can be observed that the addition of an emulsifier resulted in a stronger droplet deformation.

On a trajectory close to the wall, deformed droplets could be found in the range of $1.5 \leq x/D \leq 6$. Most droplets were located in the range of $1.5 \leq x/D \leq 4$ with a deformation ratio of $24 < b < 42$, while the average

TABLE 4 Average deformation for droplets with a trajectory close to the wall ($r^* = 0.94$) or on the centreline ($r^* = 0$) with and without emulsifier at $Re_{\text{orifice}} = 1000$, $d_0 = 200 \mu\text{m}$ and $\lambda = 3.09$

r^* (-)	Emulsifier fraction (wt.%)	Interfacial tension in equilibrium γ ($\text{mN} \cdot \text{m}^{-1}$)	Deformation ratio b (-)	Deformation ratio b_{r^*} (-)
0	0.5	3.20 ± 0.04	15.3 ± 3.1	3.3 ± 1.2
0	0	15.52 ± 0.20	4.6 ± 1.3	
0.94	0.5	3.20 ± 0.04	82.5 ± 6.9	2.4 ± 0.4
0.94	0	15.52 ± 0.20	34.0 ± 5.4	

deformation ratio of all droplets on a trajectory close to the wall was $b = 34.0 \pm 5.4$. Only individual droplets were found further downstream, representing droplets that were potentially pulled back in the jet by the surrounding backflow, and deformed during this process. This phenomenon was already described by Mutsch et al.^[15] Similar to the results with added emulsifier, a tendency of an increasing deformation ratio with an increasing distance from the orifice exit can be found for droplets on a trajectory close to the wall. In general, the presence of an emulsifier results in a stronger deformation of the droplets on a trajectory close to the wall.

The influence of an emulsifier on the deformation ratio b can be described with the parameter b_{r^*} , which is defined as follows:

$$b_{r^*} = b(\text{with emulsifier}, r^*) / b(\text{without emulsifier}, r^*) \quad (11)$$

where b_{r^*} represents the ratio of the deformation ratio b of the droplets with added emulsifier to droplets without emulsifier on a trajectory r^* . A relative deformation ratio b_{r^*} of 3.3 ± 1.2 was found for the trajectory on the centreline. The trajectory close to the wall resulted in relative deformation ratio b_{r^*} of 2.4 ± 0.4 . Droplet deformation is increased by the presence of emulsifier with the effect being slightly more pronounced on the centreline.

3.2.3 | Influence of viscosity ratio

Taylor^[4] has shown that in emulsions under small stresses, the droplet deformation is proportional to the capillary number Ca while the slope depends on the viscosity ratio λ . Taylor showed that the influence of the interfacial tension on the deformation increases with a decreasing viscosity ratio. The correlation was only proven for small constant stresses under laminar flow conditions. Simulations of Walzel^[10] showed that this correlation may also be applicable to the droplet deformation behaviour during high-pressure homogenization. The influence of the

interfacial tension on the droplet deformation should increase with decreasing viscosity ratio.

The deformation ratios of droplets of two viscosity ratios at two interfacial tension levels are shown in Table 5. It was found that the deformation ratio of droplets in an emulsion with a viscosity ratio of 3.09 is larger compared to droplets in an emulsion with a viscosity ratio of 25. Furthermore, the deformation ratio increased at both investigated viscosity ratios when an emulsifier was added. When investigating the influence of the presence of emulsifier molecules on the droplet deformation ratio at different viscosity ratios, the relative deformation ratio b_λ can be used:

$$b_\lambda = b(\text{with emulsifier}) / b(\text{without emulsifier}) \quad (12)$$

where the ratio of the deformation ratio of droplets with added emulsifier and droplets without added emulsifier is calculated. The resulting deformation and relative deformation ratios are presented in Table 5.

Droplets in an emulsion with a viscosity ratio of 3.09 resulted in a relative deformation ratio of $b_\lambda = 3.2 \pm 0.6$. In comparison, droplets in an emulsion with a viscosity ratio of 25 showed a lower relative deformation ratio of $b_\lambda = 1.9 \pm 0.5$.

3.3 | Stress history

Here, the stress history of droplets on several trajectories is determined using CFD simulations to explain the differences in droplet deformation when altering the droplet trajectory.

Droplets are subjected to elongation strain and shear stress in the inlet and in the orifice of a high-pressure homogenizer. Feigl et al.^[13] and Hövekamp^[14] demonstrated that the stresses differ along the streamlines in the process and are highest in the wall region. The measured differences in droplet deformation suggest that both, the maximum values and the integral values of strain rate and shear rate, decrease concurrently with the dimensionless radius r^* . In all diagrams within this

TABLE 5 Average deformation for droplets with a trajectory on the centreline ($r^* = 0$) with and without emulsifier for different viscosity ratio values at $Re = 2000$ und $d_0 = 200 \mu\text{m}$

	Viscosity ratio λ (–)	Interfacial tension in equilibrium γ ($\text{mN} \cdot \text{m}^{-1}$)	Deformation ratio b (–)	Relative deformation ratio b_λ (–)
With emulsifier	3.09	3.20 ± 0.04	24.9 ± 3.2	3.2 ± 0.6
Without emulsifier	3.09	15.52 ± 0.20	7.8 ± 1.0	
With emulsifier	25	2.77 ± 0.15	5.9 ± 0.9	1.9 ± 0.5
Without emulsifier	25	13.80 ± 0.22	3.0 ± 0.7	

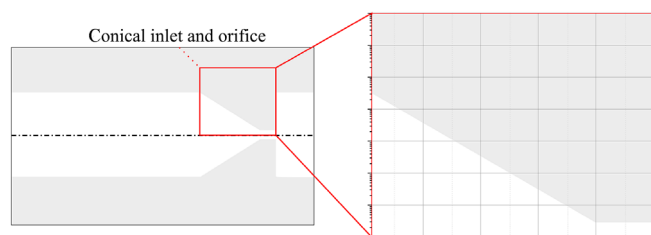


FIGURE 7 Cross-sectional view of the used orifice with the highlighted area used to evaluate the stress load in the following figures. The left side of the highlighted area has the same scaling as in the following figures

subchapter, the cross-section of the geometry according to Figure 7 is shown in the background of the diagrams for better understanding.

Figure 8A shows the elongation rate $\dot{\epsilon}$ at a Reynolds number of 1000, which represents the experimental conditions used in Section 3.2.1, plotted over the normalized distance to the orifice exit on three different streamlines distributed over the cross-section of the geometry. In the background, the cross-section of the geometry is shown in grey for better understanding. The area of the conical inlet and the orifice are considered for evaluation.

At the entrance to the conical inlet, the strain rate on all three streamlines is about $\dot{\epsilon} = 20 \text{ s}^{-1}$. It increases to a maximum value, which is reached at the beginning of the narrowest cross-section. The two inner trajectories ($r^* = 0$ and $r^* = 0.47$) are in a similar range for $x/D \leq -2$ with maximum values of $\dot{\epsilon} = 1.02 \cdot 10^4 \text{ s}^{-1}$ for $r^* = 0$ and $\dot{\epsilon} = 1.33 \cdot 10^4 \text{ s}^{-1}$ for $r^* = 0.47$, while the values of the trajectory close to the wall ($r^* = 0.94$) reach a maximum value of $\dot{\epsilon} = 1.28 \cdot 10^5 \text{ s}^{-1}$. At the entrance to the narrowest cross-section, the strain rate on the outer trajectory decreases. This is probably due to the streamline following the vena contracta, which is formed at this point. Following the peak, the curves take an s-shaped course, which ends in a local minimum shortly before the end of the orifice at $x/D \approx -0.1$. The values increase again afterward. The elongation rate is in a similar range in the region of the orifice drilling hole ($x/D > -2$) for all three streamlines. The reason for the local minimum

could be the change of the flow direction in y- and z-directions. This is due to the parabolic flow profile in a change of the flow variables, which were taken into account in the calculation of the elongation rate. Wall effects are only pronounced in close wall vicinity.

To evaluate the total elongation strain over the residence time on the streamline, the elongation rate is integrated over the residence time and afterward normalized with respect to the value of the outer trajectory ($r^* = 0.94$). The results are represented in Figure 8B, showing that the elongation on the two inner trajectories ($r^* = 0$ and $r^* = 0.47$) over the residence time hardly differs, but is significantly lower than the integral elongation rate on the near-wall trajectory. The values are in the order of 10% of those calculated for the outer trajectory, which approximately coincides with the difference of the maximum values.

The evaluation of the shear rate is carried out similarly to that of the strain rate. The shear rate, plotted over the normalized distance to the orifice outlet in Figure 9A, increases for all trajectories with a similar slope until shortly before entering the narrowest cross-section. In contrast to the elongation rate, the shear rates of the three streamlines already differ significantly from each other at the entry into the conical inlet. The values increased with increasing r^* : from $\dot{\gamma} = 1.90 \cdot 10^{-1} \text{ s}^{-1}$ ($r^* = 0$) via $\dot{\gamma} = 3.18 \cdot 10^1 \text{ s}^{-1}$ ($r^* = 0.47$) to $6.66 \cdot 10^1 \text{ s}^{-1}$ ($r^* = 0.94$). Shortly before entering the orifice, the shear rate of the inner two trajectories drops, while the shear rate of the outer trajectory continues to increase up to the maximum value of $\dot{\gamma} = 2.82 \cdot 10^5 \text{ s}^{-1}$. The collapse of the shear rate on the inner two trajectories can be explained as a result of the velocity gradients falling to 0 due to the uniform velocity field at the entrance to the cylindrical part of the orifice. Due to the wall adhesion, the gradient of the velocity in the flow direction towards the centreline on the outer trajectory is so high that it outweighs the influences of the other gradients. After the collapse of the values on the two inner trajectories, they increase again and each reaches its maximum values at an $x/D = -2$ at a value of $\dot{\gamma} = 5.20 \cdot 10^1 \text{ s}^{-1}$ ($r^* = 0$) and a value of $4.82 \cdot 10^3 \text{ s}^{-1}$ ($r^* = 0.47$). After reaching the

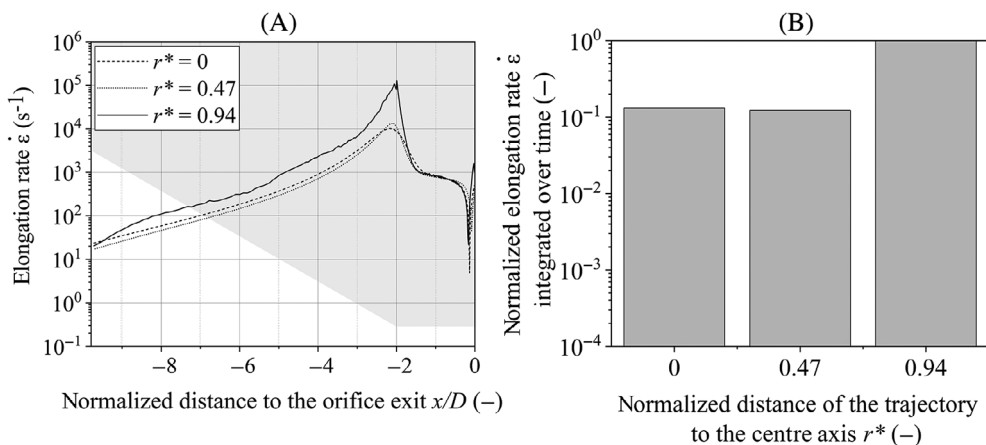


FIGURE 8 Elongation rate of different streamlines at $Re_{\text{orifice}} = 1000$ (A) plotted over the normalized distance to the orifice exit and (B) integrated over the residence time in the conical part and the orifice drilling hole

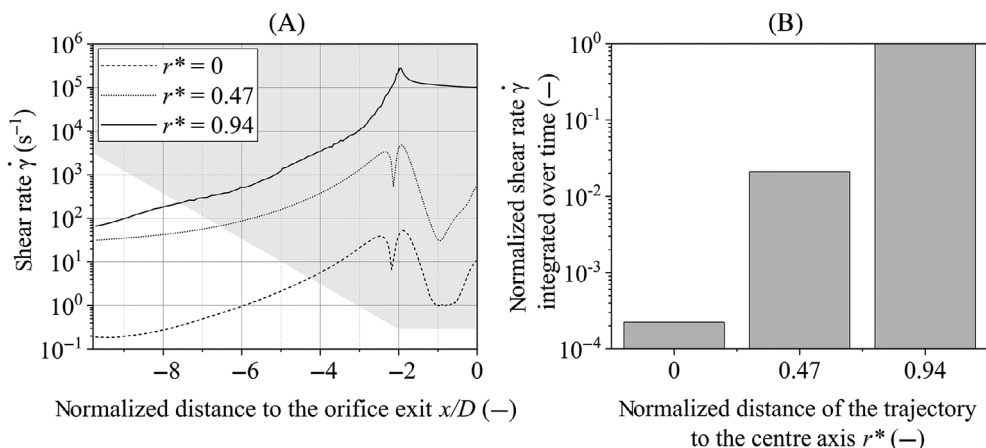


FIGURE 9 Shear rate of different streamlines at $Re_{\text{orifice}} = 1000$ (A) plotted over the normalized distance to the orifice exit and (B) integrated over the residence time

maximum value, all three curves drop. However, there is a further increase in the shear rate on the two inner trajectories within the narrowest cross-section, which again can be explained by the change in flow direction in the two directions perpendicular to the main flow axis. Due to the laminar parabolic flow profile, near the wall ($r^* = 0.94$), this effect is so reduced that it can no longer be seen in the course of the shear rate.

For Figure 9B, the shear rate was integrated over time and then normalized for the three trajectories. Again, the integration provided an agreement of the normalized values with the maximum values of the shear rate. The integral values of the shear rate increased with increasing r^* . On the centre trajectory, the fraction compared to the edge trajectory is $2.24 \cdot 10^{-4}$. For $r^* = 0.47$, the fraction is $2.09 \cdot 10^{-2}$.

Comparing the maximum values of strain rates and shear rates on the trajectories at $r^* = 0$ and $r^* = 0.94$ in Figure 10A,B, it becomes obvious that the influences of the stresses vary depending on the location within the geometry. While the elongation rate in the centre of the geometry clearly dominates over the entire distance considered, in the wall region, the shear rate is predominant.

In this area, the elongation strain plays a minor role, although the difference in the values up to $x/D = -2$ is less pronounced than in the centre of the geometry. For $x/D > -2$, the influence of the shear rate in the near-wall region increases significantly.

The capillary number, calculated according to Equations (3) and (4), is considered as a parameter for the deformation of the droplets. Since the influence of elongation and shear varies depending on the trajectory, the critical capillary number is calculated separately for the trajectory close to the wall and the centreline trajectory. Figure 11 shows the critical capillary number as a function of the parameter α for a viscosity ratio of $\lambda = 3$ according to Windhab et al.^[5] The parameter α can be described for mixed flow conditions as a function of the shear rate and elongation rate:

$$\alpha = \frac{|\dot{\epsilon}|}{|\dot{\epsilon}| + |\dot{\gamma}|} \quad (13)$$

The critical capillary number was determined for an interfacial tension of $3.2 \text{ mN} \cdot \text{m}^{-1}$ and a Reynolds number of 1000. For this purpose, the time-averaged stress

FIGURE 10 Shear rate and strain rate plotted over the normalized distance to the orifice exit for (A) $r^* = 0$ and (B) $r^* = 0.94$

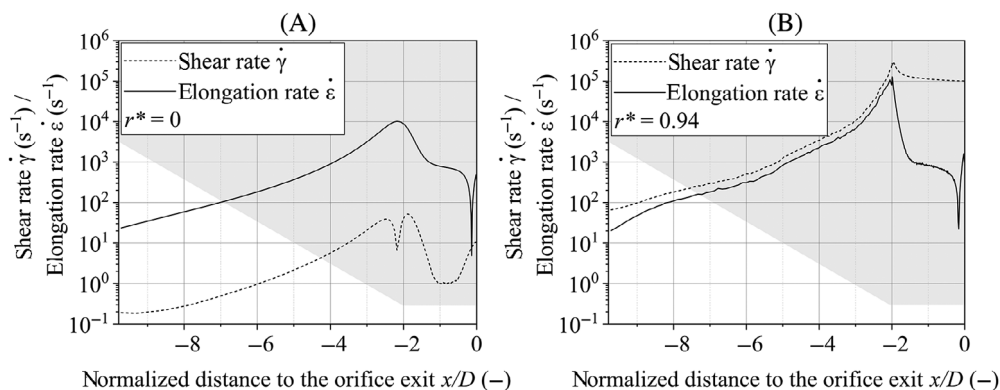


FIGURE 11 Critical capillary number plotted over α for a viscosity ratio of $\lambda = 3$ according to Windhab et al.^[5] The critical capillary number is marked in red for $r^* = 0$ and $r^* = 0.94$ at $Re = 1000$

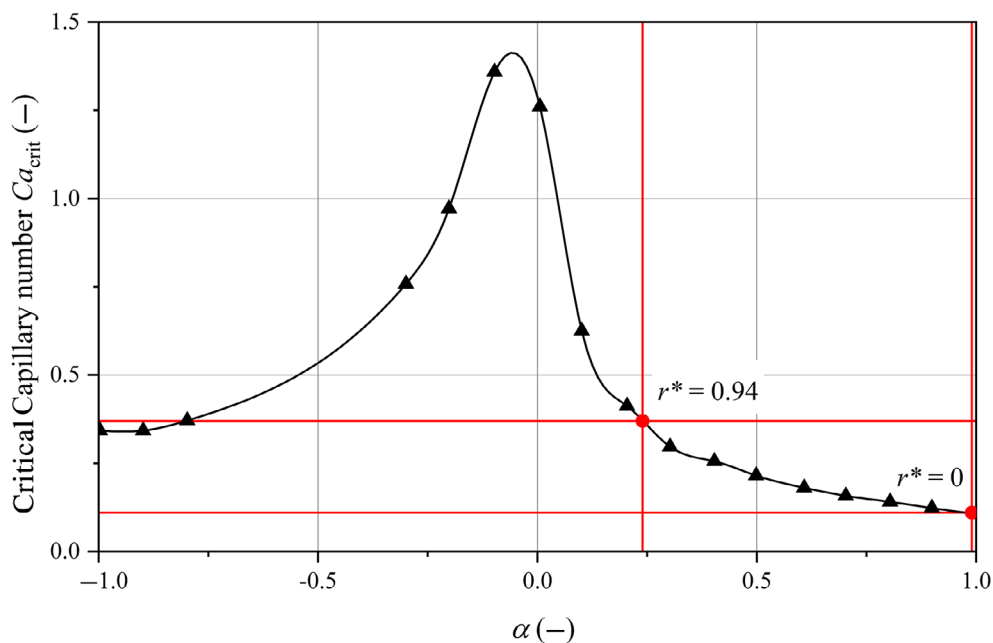


TABLE 6 Stress values and resulting α for different streamlines at $Re = 1000$

r^* (-)	$\dot{\epsilon}$ (s^{-1})	$\dot{\gamma}$ (s^{-1})	α (-)
0	250.97	1.40	0.99
0.94	445.91	1449.53	0.24

values along the streamlines are considered. The values can be taken from Table 6.

Using the parameter α , the critical capillary number for the streamlines can be determined from Figure 11. For $r^* = 0$, a value of $Ca_{crit} = 0.11$ and for $r^* = 0.94$, a value of $Ca_{crit} = 0.37$ are obtained. These values are assumed to be constant along the streamlines.

Figure 12A shows the dependency of the capillary number on the normalized distance to the orifice outlet calculated for a droplet diameter of $200 \mu m$ and an interfacial tension of $3.2 mN \cdot m^{-1}$. The critical capillary number

on the inner trajectory ($r^* = 0$) is exceeded in a range of the normalized distance of about $-4.2 < x/D < -1$. In comparison, the critical capillary number on the trajectory near the wall ($r^* = 0.94$) is exceeded earlier ($x/D = -4.8$) and is not undercut again. Looking at the capillary number profile for a droplet diameter of $20 \mu m$ in Figure 12B, the curves are shifted downwards by a factor of 10 since the droplet diameter is linearly considered in the calculation of the capillary number. While the stresses near the wall are sufficient to exceed the critical capillary number over a considerable distance up to a maximum factor of 10 ($Ca = 10 \cdot Ca_{crit}$), the critical capillary number on the centreline is only slightly exceeded in the area of the entry into the narrowest cross-section. It is therefore assumed that small droplets in the interior of the geometry undergo little deformation. Since the capillary number is inversely proportional to the interfacial tension (cf. Equation 3), the curves increase with decreasing interfacial tension and vice versa. For a decrease in

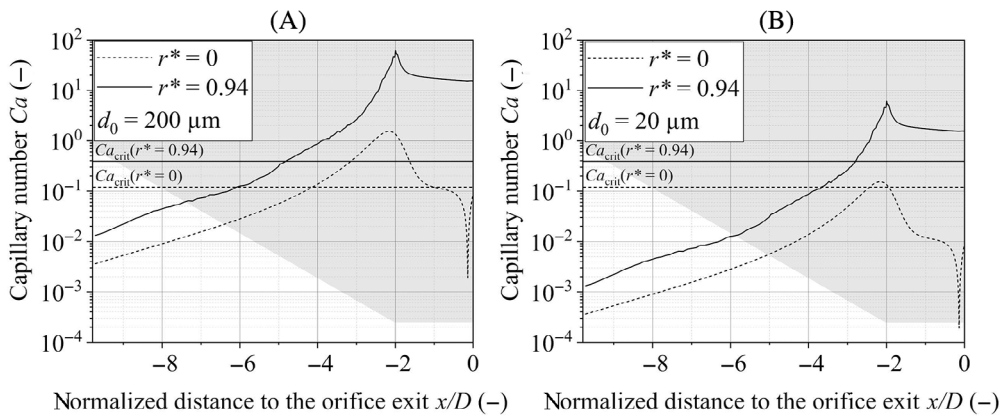


FIGURE 12 History of the capillary number calculated for $\gamma = 3.2 \text{ mN} \cdot \text{m}^{-1}$ on different trajectories. The corresponding critical capillary number was calculated for $\lambda = 3$ for (A) a droplet diameter d_0 of $200 \mu\text{m}$ and (B) a droplet diameter d_0 of $20 \mu\text{m}$

the interfacial tension by a factor of 10, the capillary number curve would be shifted upward by the same factor. This significantly increases the area in which the critical capillary number is exceeded. This effect is more pronounced for the inner trajectory than for the near-wall trajectory as a result of the ratio of the capillary number on the trajectory to the critical capillary number.

4 | DISCUSSION

The results of this study show that droplets that flow through a high-pressure homogenizer orifice on a trajectory close to the wall result in smaller droplets compared to droplets that flow close to the centreline. The effect is significant for emulsions of a viscosity ratio greater than 3, which is in agreement with the findings of Mutsch et al.^[15] Regarding the lowest investigated viscosity ratio of $\lambda = 1.15$, no influence of the droplet trajectory on the droplet size distribution could be observed.

Possibly, the stresses on both trajectories were high enough to cause a pronounced droplet deformation in the orifice for low viscous droplets ($\lambda < 3$), which should facilitate the breakup of the deformed droplets. Droplet breakup should be most efficient if the thread diameter is about the size of the smallest vortex size as proposed for spherical droplets in isotropic turbulence by Hinze.^[23] For higher viscosity ratios, a less pronounced deformation of droplets flowing on the centreline would be expected. The visualized droplets confirmed this expectation, as droplets on a trajectory close to the wall were more deformed compared to droplets on the centreline. Moreover, the droplet deformation decreased with an increasing viscosity ratio. Furthermore, the deformation of droplets following close to the wall increased downstream of the orifice exit, which further increased the difference in droplet deformation. A possible explanation for the increase in deformation could be that these droplets are probably exposed to additional forces when they

are on the edge of the core area of the jet and enter the shear layer. Time effects in the deformation may also not be excluded. In general, droplets on a trajectory close to the wall resulted in a larger scattering of the droplet deformation ratio, as probably even slight deviations in the trajectory result in greater deviations of the stress history. The more pronounced deformation can be supported by the CFD simulations, which have shown that the shear stress and the elongation strain in the near-wall region are significantly higher than the stresses in the centre of the geometry. This is in agreement with the experimental results of Bisten et al.^[24] When comparing the stress history on a trajectory on the centreline ($r^* = 0$) and a trajectory in the middle ($r^* = 0.47$), it can be noticed that the integrated and normalized elongation stress is almost equal. Only higher values of integrated and normalized shear stress can be found on the middle trajectory ($r^* = 0.47$) compared to the trajectory on the centreline ($r^* = 0$). Nevertheless, the stresses are still much lower compared to those found on the trajectory close to the wall. A severe increase in the stress load is expected if the trajectory is getting closer to the wall. Thus, the stress history of trajectories surrounding the centreline is more homogeneous, which again is consistent with the experimental findings of Bisten et al.^[24]

Furthermore, the results indicate that a smaller number of large droplets were produced if the droplets flowed on a trajectory close to the wall, which resulted in a narrower droplet size distribution. This may be an indication that larger droplets, which can be deformed more easily than smaller droplets, are broken up more efficiently on a trajectory close to the wall due to the pronounced deformation. The CFD simulations have shown that the critical capillary number is exceeded for a longer time for larger droplets compared to smaller droplets and thus a stronger deformation can be expected. Although the droplets are exposed to supercritical stresses ($Ca > Ca_{\text{crit}}$), the droplet breakup is still dominated by the turbulent viscous and inertial forces in the turbulent

shear layer of the jet, as the deformation time of the droplet is too short to achieve critical deformation for droplet breakup. This is underlined by the findings of Mutsch et al.^[15] in a scaled system. As also the time between leaving the orifice and entering the turbulent shear layer is short, the deformed droplets relax only slightly. This is also described by Mutsch et al.^[15] Even filaments with a deformation ratio of $b > 100$ are still too thick to result in droplets within the size range of $1 \mu\text{m}$ with a laminar breakup mechanism. However, the lower capillary pressure in the cylindrical part of the deformed filament compared to an undeformed droplet may facilitate additional droplet deformation caused by vortices in the shear layer. It may be assumed that weaker vortices can thus cause a pronounced deformation of the droplet into a complex three-dimensional shape. Furthermore, the deformed filament can interact with more vortices compared to a spherical droplet entering the shear layer, as the front part of the deformed filament might already enter the shear layer while the back part is still in the drilling hole of the orifice. The proposed hypothesis that smaller droplets emerge from droplets that flow close to the wall compared to droplets flowing on the centreline independent of the viscosity ratio cannot be confirmed for emulsions with a low viscosity ratio.

Droplet deformation can be increased by either increasing the stresses or by decreasing the shape-maintaining forces—in this case, the capillary pressure—by decreasing the interfacial tension with an emulsifier whereby the viscosity ratio is maintained. The experiment confirmed an increasing droplet deformation ratio when adding an emulsifier for both trajectories. The CFD simulations also show that the critical capillary number is exceeded for a longer time if the interfacial tension is lowered. However, the measured values of the increase in droplet deformation were less pronounced than expected. A possible explanation for this finding is that the emulsifier did not adsorb fast enough at the newly created interface during droplet deformation, as described by Brösel and Schubert^[8] and Riechers et al.,^[25] which results in interfacial tensions above the equilibrium value. We also expect Gibbs–Marangoni effects to cause an uneven interfacial tension distribution at the deformed droplets' interfaces, which will influence the deformation of the droplets. The latter would also explain the comet-like shape of deformed droplets as described in Mutsch et al.^[15] The time constants for droplet deformation and emulsifier adsorption interfere in high-pressure homogenization. In the experimental setup used in this study, emulsifier diffusion and adsorption effects could not be scaled, as discussed by Preiss et al.^[19] It is assumed that the addition of an emulsifier during a high-pressure homogenization process in the original scale has a

smaller influence on the droplet deformation. Derived from the previously described findings, it can be expected that an emulsifier has a smaller influence on the droplet deformation ratio of droplets on a trajectory close to the wall compared to droplets on the centreline, as more interface is created. Thus, the emulsifier is more diluted at the interface during the deformation process, and the deformation is expected to be closer to a system without any emulsifier. An initial tendency for the previously established expectation to occur can be observed when comparing the parameter b_{r^*} of the two trajectories. Nevertheless, due to the high standard deviation of the parameter b_{r^*} no final statement can be conducted on the influence of the trajectory on the emulsifier adsorption.

Furthermore, it was hypothesized that the findings of Taylor^[4] on the influence of the interfacial tension and viscosity ratio on droplet deformation, which were performed under constant stresses, are also valid for droplet deformation in fast-changing stress and strain fields—as found in high-pressure homogenizer orifices. Comparing the relative deformation ratio b_λ of droplets in an emulsion with a viscosity ratio of 3.09 and 25 shows that this hypothesis could be approved as the relative deformation ratio b_λ of droplets in the emulsion with a viscosity ratio of 25 is lower compared to droplets with the lower viscosity ratio. However, the influence of the viscosity ratio on the droplet deformation when altering the interfacial tension is not pronounced, as again, large standard deviations were found, and the interfacial tension is expected to be higher than the equilibrium value and unevenly distributed due to the too slow emulsifier adsorption in fast droplet deformation experiments. This may have also decreased the influence of the viscosity ratio on the droplet deformation when adding an emulsifier. As a stronger deformation was observed for droplets with a viscosity ratio of 3.09, it can be concluded that the uneven emulsifier distribution at deformed droplets' interphases is probably more pronounced for lower viscosities/higher deformation rates. In the work of Taylor^[4] and Walzel^[10] the influence of the viscosity ratio on droplet deformation when altering the interfacial tension was more pronounced, possibly due to the fact that Taylor increased the droplet deformation slowly and gradually and that no emulsifier was present, which leads to the assumption that, similarly as in the simulation of Walzel, the interfacial tension was constant at the whole interface.

In general, it can be expected that the effects of the droplet trajectory on the droplet deformation and on breakup are also found in an original scale high-pressure homogenizer with flat valves. In the industrial process, higher pressure losses are usually applied, which results in higher capillary numbers of the droplets and higher Reynolds numbers of the flow. Furthermore, in the

industrial process, the ratio of the droplet diameter d_0 to the characteristic length D of the disruption unit is smaller by an order of 10 compared to the setup used in the presented laboratory experiment, which reduces the capillary number and thus the deformation. However, the reduced residence time in the original scale also inhibits droplet relaxation. For example, the residence time in the used scaled disruption unit is about 10 times the residence time in the original scale disruption unit. It is, therefore, to be expected that the effects found here will also occur in industrial processes with other size ratios and geometries, although probably to a different extent. In flat valves (as typically found in industrially used high-pressure homogenizers), a comparable flow profile is formed with laminar flow in the inlet and a turbulent jet downstream of the constriction.^[26] Nevertheless, it has to be taken into account that only a minor fraction of the droplets are flowing on trajectories close to the wall—especially if a fully developed flow with a parabolic flow profile is present—which can reduce the effect of the droplet trajectory on the resulting droplet size distribution in the industrial process.

5 | CONCLUSIONS

The main goal of the current study was to determine the influence of the droplet trajectory on the resulting droplet size distribution and explain the effects by determining the droplets' deformation prior to their breakup as a result of the stress history droplets experience when following defined trajectories. Changes in droplet deformation were subsequently correlated with the stress history on the trajectory.

The study has shown that, in case of a viscosity ratio greater than 3, droplets travelling on a trajectory close to the wall resulted in smaller droplets compared to droplets on the centreline trajectory. Moreover, a narrower droplet size distribution was found for droplets that flowed on a trajectory close to the wall, resulting mainly from less big droplets in the distribution. This confirms the high importance of the deformation of the high-viscous droplets when flowing through the narrowest point of dispersion units. The effect is significantly reduced for emulsions of smaller viscosity ratios ($\lambda = 1.16$ in this study).

The changes in the droplet size distribution could be explained by the more pronounced deformation of droplets that travelled on a trajectory close to the wall compared to droplets on the centreline. The CFD simulations have shown that the stress load on a trajectory close to the wall is significantly higher compared to a trajectory on the centreline and the shear forces dominated the stress history. Thus, a stronger deformation was expected

based on the simulated stress history. This could be confirmed with experimentally visualized droplets.

The droplet deformation can also be increased by reducing the shape-maintaining forces by reducing the interfacial tension with an emulsifier. It was observed that the addition of an emulsifier resulted in a stronger droplet deformation for both trajectories. However, the effect was smaller than expected, probably because the emulsifier molecules did not adsorb fast enough at the newly created interface during deformation and Gibbs–Marangoni effects. Besides, it was observed that the influence of the interfacial tension on the droplet deformation is more prominent at lower viscosity ratios, which was already experimentally shown for low and slow deformation^[4] as well as in simulations^[12] with fast-changing stresses as applied in this study. However, the effect was again less prominent than that expected from the work of Taylor^[4] and Mutsch et al.^[12] due to the discussed emulsifier adsorption kinetics-induced effects.

ACKNOWLEDGEMENTS

The authors thank Jürgen Kraft, Markus Fischer, Tillman Finger, and Annette Berndt for designing the test site and providing assistance during the experiments. Furthermore, the authors thank Christian Geuter for performing the particle size measurements. We thank Dieter Waltz and Peter Fischer of the Institute of Physical Chemistry for manufacturing and Ralf Dorsner (wbk Institute of Production Science) for polishing the orifices. Further thanks go out to IOI Oleo GmbH for providing the oil and to Tillman Finger for optimizing the image processing. We also thank Peter Walzel for the fruitful discussions on the concept of this study. Last, we would like to acknowledge the financial support from the German Research Foundation (DFG) (grant numbers: 265685259 and 425332181). Open access funding enabled and organized by Project DEAL.

AUTHOR CONTRIBUTIONS

Felix Johannes Preiss: Conceptualization; formal analysis; investigation; project administration; software; supervision; visualization; writing – original draft. **Eva Rütten:** Formal analysis; investigation; software; visualization; writing – original draft. **Alexander Tröster:** Formal analysis; investigation; software; visualization; writing – original draft. **Volker Gräf:** Formal analysis; investigation; writing – review and editing. **Heike Petra Karbstein:** Conceptualization; funding acquisition; project administration; supervision; writing – review and editing.

NOMENCLATURE

Symbols

d droplet diameter (m)

D	orifice diameter (m)
d_0	diameter of the undeformed droplet (m)
d_1	length of major axis of the emerging ellipsoid (m)
d_2	length of minor axis of the emerging ellipsoid (m)
\dot{m}	mass flow rate ($\text{kg} \cdot \text{s}^{-1}$)
p	pressure (Pa)
r	distance of the trajectory to the centreline (m)
t	residence time (s)
\bar{u}	average velocity in x direction ($\text{m} \cdot \text{s}^{-1}$)
\bar{v}	average velocity in y direction ($\text{m} \cdot \text{s}^{-1}$)
\bar{w}	average velocity in z direction ($\text{m} \cdot \text{s}^{-1}$)
x	x -direction (m)
y	y -direction (m)
z	z -direction (m)

Greek letters

γ	interfacial tension ($\text{N} \cdot \text{m}^{-1}$)
$\dot{\gamma}$	shear rate (s^{-1})
$\dot{\epsilon}$	strain rate (s^{-1})
η	dynamic viscosity ($\text{Pa} \cdot \text{s}$)
ρ	density ($\text{kg} \cdot \text{m}^{-3}$)
τ	stresses acting on the droplet ($\text{kg} \cdot \text{m}^{-1} \cdot \text{s}^{-2}$)

Subscripts

b_p	backpressure
c	continuous phase
in	inlet

Dimensionless numbers

b_{r^*}	relative deformation ratio based on the trajectory
b_0	deformation ratio according to Cox
b_λ	relative deformation ratio based on the viscosity ratio
b	deformation ratio
Ca	capillary number
r^*	dimensionless location of the trajectory in the inlet channel
Re	Reynolds number
Th	Thoma number
λ	viscosity ratio

DATA AVAILABILITY STATEMENT

Data available on request from the authors

ORCID

Felix Johannes Preiss  <https://orcid.org/0000-0002-9841-9197>

REFERENCES

- [1] A. Håkansson, *Annu. Rev. Food Sci. T.* **2019**, *10*, 239.
- [2] N. Vankova, S. Tcholakova, N. D. Denkov, I. B. Ivanov, V. D. Vulchev, T. Danner, *J. Colloid Interf. Sci.* **2007**, *312*, 363.
- [3] G. I. Taylor, *P. R. Soc. A* **1932**, *138*, 41.
- [4] G. I. Taylor, *P. R. Soc. A* **1934**, *146*, 501.
- [5] E. J. Windhab, M. Dressler, K. Feigl, P. Fischer, D. Megias-Alguacil, *Chem. Eng. Sci.* **2005**, *60*, 2101.
- [6] R. G. Cox, *J. Fluid Mech.* **1969**, *37*, 601.
- [7] J. J. Elmendorp, *Polym. Eng. Sci.* **1986**, *26*, 418.
- [8] S. Brösel, H. Schubert, *Chem. Eng. Process.* **1999**, *38*, 533.
- [9] K. Kelemen, S. Gepperth, R. Koch, H.-J. Bauer, H. P. Schuchmann, *Microfluid. Nanofluid.* **2015**, *19*, 1139.
- [10] P. E. Walzel, *Chem. Eng. Technol.* **2017**, *40*, 405.
- [11] B. Kalb, R. G. Cox, R. St. John Manley, *J. Colloid Interf. Sci.* **1981**, *82*, 286.
- [12] B. Mutsch, P. Walzel, C. J. Kähler, *ChemEngineering* **2021**, *5*, 32.
- [13] K. Feigl, S. F. M. Kaufmann, P. Fischer, E. J. Windhab, *Chem. Eng. Sci.* **2003**, *58*, 2351.
- [14] T. B. Hövekamp, Ph.D. Thesis, ETH Zürich (Zürich, Switzerland) 2002.
- [15] B. Mutsch, F. J. Preiss, T. Dagenbach, H. P. Karbstein, C. J. Kähler, *ChemEngineering* **2021**, *5*, 31.
- [16] A. Håkansson, L. Fuchs, F. Innings, J. Revstedt, C. Trägårdh, B. Bergenstahl, *Chem. Eng. Sci.* **2012**, *71*, 264.
- [17] A. Shah, P. Thool, K. Sorathiya, H. Prajapati, D. Dalrymple, A. T. M. Serajuddin, *Drug Dev. Ind. Pharm.* **2018**, *44*, 215.
- [18] Selecting an appropriate particle absorption for laser diffraction particle size calculations, <https://www.malvernpanalytical.com/de/learn/knowledge-center/technical-notes/TN101104SelectingParticleAbsorbtionLaserDiffractio> (accessed: August 2021).
- [19] F. J. Preiss, B. Mutsch, C. J. Kähler, H. P. Karbstein, *ChemEngineering* **2021**, *5*, 7.
- [20] F. J. Preiss, T. Dagenbach, M. Fischer, H. P. Karbstein, *ChemEngineering* **2020**, *4*, 60.
- [21] M. Schlender, K. Minke, B. Spiegel, H. P. Schuchmann, *Chem. Eng. Sci.* **2015**, *131*, 162.
- [22] F. J. Preiss, M. Hetz, H. P. Karbstein, *Chem.-Ing.-Tech.* **2021**. <https://doi.org/10.1002/cite.202100104>.
- [23] J. O. Hinze, *AIChE J.* **1955**, *1*, 289.
- [24] A. Bisten, D. Rudolf, H. P. Karbstein, *Microfluid. Nanofluid.* **2018**, *22*, 607.
- [25] B. Riechers, F. Maes, E. Akoury, B. Semin, P. Gruner, J.-C. Baret, *P. Natl. Acad. Sci. USA* **2016**, *113*, 11465.
- [26] F. Innings, C. Trägårdh, *Exp. Therm. Fluid Sci.* **2007**, *32*, 345.

How to cite this article: F. J. Preiss, E. Rütten, A. Tröster, V. Gräf, H. P. Karbstein, *Can. J. Chem. Eng.* **2022**, *1*. <https://doi.org/10.1002/cjce.24363>